Static and dynamic FE analysis of an RC protective structure dedicated to snow avalanche mitigation

Isabelle Ousset, David Bertrand, Michael Brun, Emmanuel Thibert, Ali Limam, Mohamed Naaim

Static and dynamic FE analysis of an RC protective structure dedicated to snow avalanche mitigation

I. Ousset [a,b,*], D. Bertrand [c], M. Brun [c], E. Thibert [a,b], A. Limam [c], M. Naaïm [a,b]

[a] Irstea, UR ETGR, Centre de Grenoble, 2 rue de la Papeterie — BP 76, F-38402 Saint-Martin-d'Hères, France
[b] Univ. Grenoble Alpes, F-38041 Grenoble, France
[c] INSA Lyon, LGCIE, 20 avenue Albert Einstein, F-69621 Villeurbanne, France

Snow avalanches threaten more and more people and different types of structures in mountainous areas. This study focuses on a protective RC (reinforced concrete) structure consisting of an L shaped wall. The objective of this paper is to calibrate and validate a 2D FE (Finite Element) model in order to explore the behavior of such RC structures loaded by pressure time signals caused by snow avalanche flows and to assess their vulnerability. Four concrete constitutive laws were tested to accurately describe the total collapse of the structure obtained from a pushover test carried out on a physical 1/6 scale model. Only two of four allowed converging up to the collapse of the wall. Then, the FE model was used to investigate the mechanical response of the wall under dynamic avalanche loading. The result shows that three types of structural responses can occur depending on the impulse of the loading signal: quasi static, dynamic or impulsive. In the case of dense snow avalanche loadings, the response of the wall can be described as quasi static. Nevertheless, this conclusion should be interpreted cautiously. Indeed, avalanche im pulses depend on many factors (type of avalanche, density, temperature, etc.) underlining that different structural responses might be expected.

1. Introduction

Avalanche hazard threatens structures and buildings in mountainous regions, where the lack of space and urbanization development continu ously increase the vulnerability of human communities. Within the framework of risk analysis, these communities must take into account not only the description of this natural hazard, but also the physical vulnerability of the civil engineering structures exposed (buildings, pro tective devices, etc.).

Today, civil engineering structures exposed to snow avalanches are mostly designed considering static loadings involving large safety factors (Ancey, 1996; Givry and Perfetini, 2006). The latter highlight the lack of knowledge on the effects of the loading generated by a snow flow. However, during the 1999 and 2005 avalanche events, significant parts of defense structures were destroyed in Taconnaz (Chamonix valley). Berthet Rambaud et al. (2007), suggested that static design approaches seem to underestimate the potential effect of the snow flow damage.

In the last few decades, research projects (such as the European SATSIE, IRASMOS, PRANE, OPALE and DYNAVAL projects) have essentially sought to improve the understanding of the processes involved in snow avalanche flows and the description of avalanche loading on structures. Some studies (Berthet Rambaud, 2004; Berthet Rambaud et al., 2007; Bertrand et al., 2010; Bonnevie et al., 2003; Bui et al., 2009; Daudon et al., 2009; etc.) investigated the effects of an avalanche on civil engineer ing structures. For actual complex structures, Berthet Rambaud et al. (2007) and Daudon et al. (2013), considered that dynamic effects caused by the avalanche loading had to be taken into account. With walls, Bertrand et al. (2010) and Favier et al. (2014), assumed that the response of reinforced concrete (RC) structures to snow avalanches can be assumed to be quasi static.

The goal of this study was to provide a better understanding of the behavior of a structure subjected to an avalanche loading using a 2D finite element (FE) model. More specifically, this paper presents the cal ibration of the FE model on experimental data obtained from a pushover test performed on a small scale physical model.

Although RC structures are very widespread in civil engineering, modeling a complex composite such as reinforced concrete still remains a frequent subject of research. Indeed, concrete consists of three constitu ents: the cement matrix, the aggregates, and the interface between the matrix and the aggregates. This complexity of the microstructure involves a specific rheology. A nonlinear behavior has to be taken into account when the elastic stress limit is reached, which is due to damage and microcracking (Mazars, 1986). Many numerical models describing this behavior have been published in the literature. At the representative ele mentary volume scale, successful concrete models have been proposed in

* Corresponding author at: Irstea, UR ETGR, Centre de Grenoble, 2 rue de la Papeterie — BP 76, F-38402 Saint-Martin-d'Hères, France Tel.: +33 4 76 76 27 64; fax: +33 4 76 51 38 03.
E-mail address: isabelle.ousset@irstea.fr (I. Ousset).

recent decades (Bazant and Oh, 1983; De Borst and Gutiérrez, 1999; etc.). Nonetheless, at the structural scale, these models require excessive com putational time. Consequently, a compromise must be found between simplicity and accuracy. The classical proposed approaches consider stan dard damage models (La Borderie, 1991; Mazars, 1986), or models based on smeared fixed crack concepts (Ile and Reynouard, 2000).

In the present paper, four constitutive laws, two based on the plasticity theory and two damage models, are tested to reproduce the strength displacement curve obtained experimentally. For steel, a clas sical law is retained according to the experimental data. Moreover, a perfect bond assumption between concrete and steel rebars is assumed.

First, a parametric study was conducted to identify the influence of the materials' properties on the structural response. The objective was to obtain numerical results in agreement with experimental data.

Finally, a synthetic triangular loading signal and a time history signal coming from in situ measurements on an obstacle inside a snow flow (Thibert et al., 2008), were applied on the modeled structure to analyze its mechanical response.

2. Materials and methods

2.1. Description of the structure

2.1.1. Taconnaz shelter

The structure considered in the present study is an RC L shaped wall. This structure is representative of existing deflection walls (Fig. 1) com prising a part of the protective device (Fig. 2) located in the Taconnaz avalanche path. This path is located in the intermediary part of the Chamonix valley below the Taconnaz glacier and is regularly impacted by snow avalanches coming from the Goûter glacier and rated as the larg est avalanche path in France. Different cottages such as the Taconnaz hamlet have been built on the alluvial fan. After being destroyed several times with previous dams proving to be insufficient, a large avalanche protective device was built in the early 1990s. Enclosing the runout zone, this complete system includes different obstacles with different functions:

- eleven deflective walls, laid out into two rows, allowing the avalanche flow to spread out when it enters the defense structure area;
- then four rows of braking mounds in a quincunx pattern, to slow down the flow and dissipate the energy;
- finally, a 14 m tall frontal terminal catching dam, which stops the progression of the avalanche.

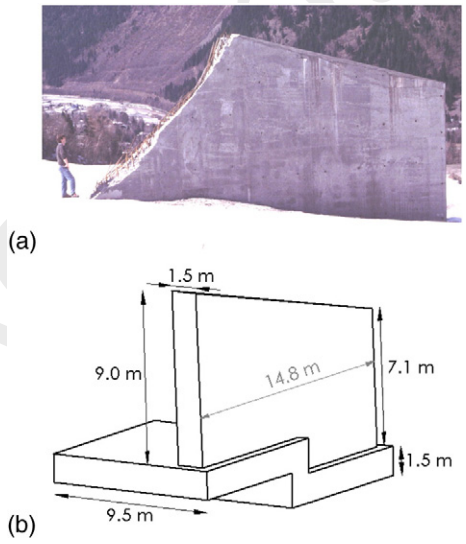

Fig. 1. (a) The actual Taconnaz deflective wall partially destroyed in 1999 (courtesy of F. Rapin — Irstea) and (b) Dimensions of the actual structure.

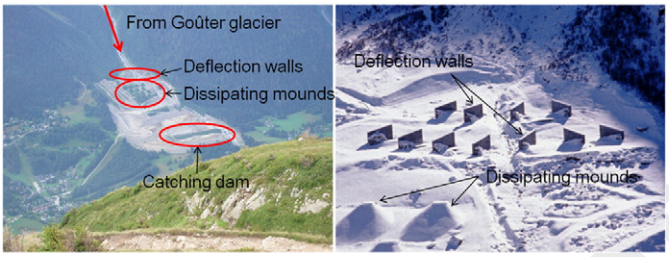

Fig. 2. Taconnaz protective device (courtesy of R. Burnet and F. Valla — Irstea).

Two of the deflective walls, located in the right extremity (in reference to the flow direction) of the protective device, were par tially destroyed by a mixed avalanche in 1999. The first wall (the lower of the two damaged walls), supported by a rock masonry structure placed behind the exposed face, was simply destroyed by a distributed pressure on the uphill wall face. The second wall (the higher of the two damaged walls) collapsed due to a combination of a distributed pressure and a localized impact likely coming from an ice or stone block. (Berthet Rambaud et al., 2007). Additional substan tial damage was again caused by a dense snow avalanche in 2005. The whole protective system was recently renewed and improved, as described in detail by Naaïm et al. (2010).

2.1.2. 1/6 scale model

To provide data for the initial explanations of the collapse of the RC structures and to investigate the initial failure mechanisms influenced by the interaction between bending and shear, laboratory tests were performed on a physical 1/6 scale model of the deflective wall, which are presented here. Given that a dynamic test was not possible, a quasi static pushover test was foreseen, considering that the behavior of a rectangular wall submitted to normal pressure had not yet been sufficiently studied (Berthet Rambaud et al., 2008).

The laboratory small scale model was defined according to the actual structure without the two foundation plates and simplifying the wall shape itself. This geometrical simplification was retained to perform experimental tests, as far as the staircase shaped base was essentially chosen to adapt the structure to the ground. The structure is then simply divided into two parts: a vertical wall and a base. The concrete is 1.6 m high, 1.0 m wide, 2.5 m long and 0.25 m thick, as specified in Fig. 3a and Table 1.

The chosen boundary conditions are a simplification of the actual sit uation: the base of the structure is clamped using a single foundation.

The wall is reinforced by steel rebars whose diameters ranged from 6 to 12 mm, placed as shown in Fig. 3a and whose characteristics are pre sented in Table 2. The reinforcement ratio is identical to that of the actual structure and the characteristics of the steel rebars were proportionally modeled. Steel layers are spaced every 12 cm in the z direction.

The numerical 1/6 scale model exposed later in Section 2.3 is fully equivalent to the experimental model.

2.1.3. Full scale model

The full scale numerical model represents the actual deflective RC wall set up on the Taconnaz protective site.

The size of the modeled structure is in that case similar to the actual structure and the geometry similar to the laboratory model, without the two foundations. It consists of concrete that is 9.6 m high, 9.0 m wide, 14.8 m long and 1.5 m thick, as specified in Fig. 3b and Table 1.

The wall is reinforced by steel rebars whose diameters range from 14 and 32 mm, placed as shown in Fig. 3b and whose characteristics are pre sented in Table 3. Steel layers are spaced every 15 cm in the z direction.

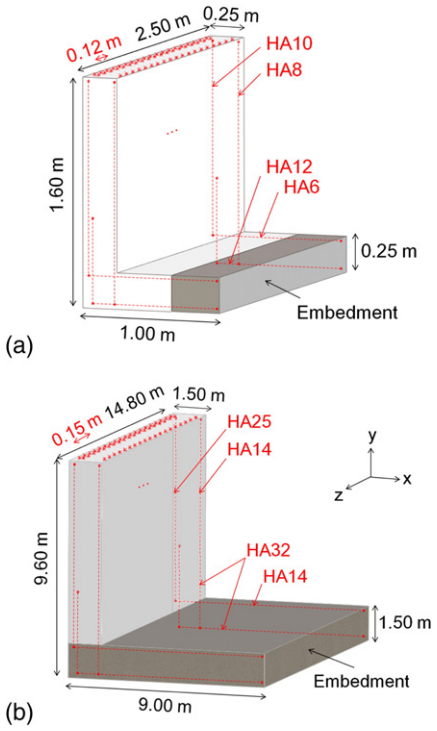

Fig. 3. (a) Experimental 1/6-scale and (b) full-scale models.

2.2. Experimental results

2.2.1. Pushover test

The experimental tests are presented in detail by Berthet Rambaud et al. (2007).

As shown in Fig. 4, the loading is applied using six hydraulic bags distributed across the upstream face. These pistons allow application of a uniform distribution of pressure varying linearly over time up to the total collapse of the wall. A reaction wall is composed of metal beams supported by set angle sections, which are themselves fixed in the test slab with prestressed steel rebars.

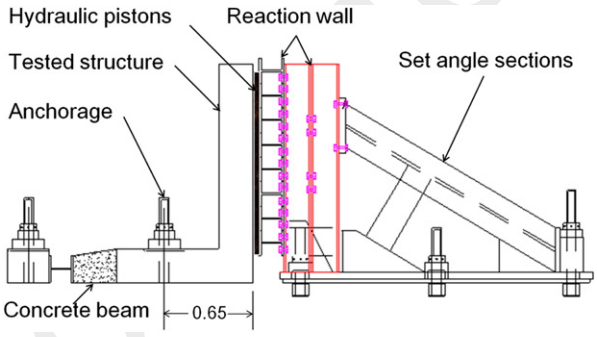

Fig. 4. Laboratory test bench.

The model is completely equipped with strain gauges positioned on the concrete wall and the steel rebars. Displacement sensors provide the horizontal deflection of the vertical wall at different locations and levels. Thus, the capacity of the structure was measured and the failure mode of the structure was observed.

These experimental tests give a complete and accurate database allowing calibration of the proposed numerical model. The experimental results are presented in Fig. 5.

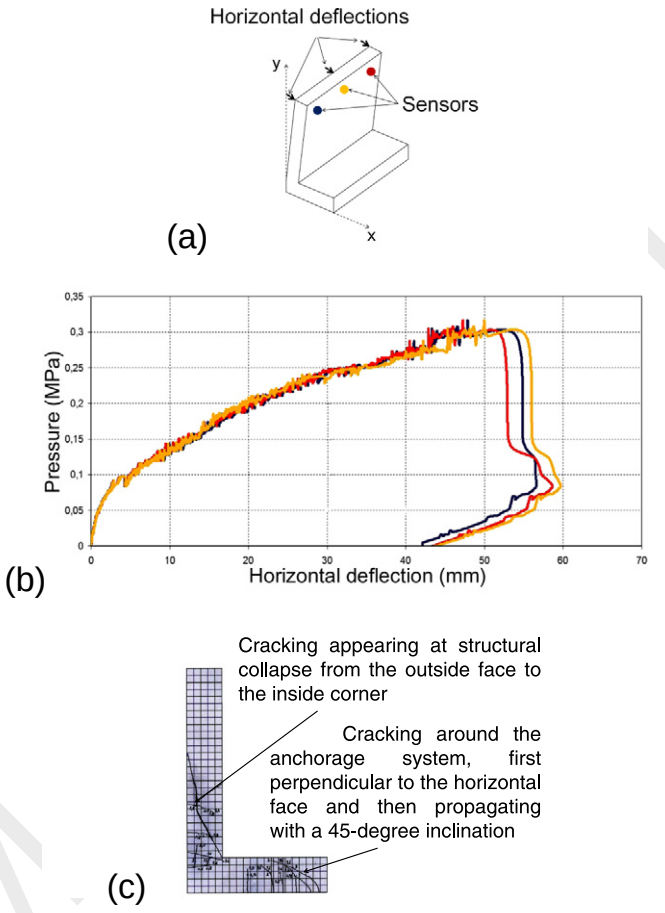

Fig. 5. Experimental results: (a) Position of the displacement sensors in the 1/6-scale model, (b) deflections measured on the top of the vertical wall and (c) cracking description at the end of the pushover test.

The load deflection curves (Fig. 5b) describe the horizontal displacement measured on the top of the vertical wall in three different points (middle and extremities, Fig. 5a) during the pushover loading.

The crack spatial distribution at the end of the test is represented in Fig. 5c. Cracks appear in two zones. The first cracks appear in the embedment at a 120 kPa pressure. These cracks, located in the right of the embedment, initially propagate vertically and then at 45° around the anchorage system. Their propagation stops at 260 kPa. Concerning the vertical wall, the first crack appears in the lower portion of the wall, near the junction at the base, at a 150 kPa pressure. Cracks then propagate towards the central part, first perpendicular to the surface of the vertical wall in accordance with the bending effect, but then progressively with an inclination. The final crack related to the collapse occurs suddenly at a 300 kPa pressure with a horizontal deflection of the vertical wall equal to 50 mm. It originates at the middle of the vertical wall on the tense face and corresponds to the rebars stopping. Then the crack extends with a 45 degree inclination to the junction between the vertical wall and the base over the compressed face, and its opening is very large (around 4 mm). In addition, the collapse appears after the rebars yield.

2.2.2. Materials properties

Experiments were conducted on the day of the test to characterize concrete and steel accurately and notably to determine their quasi static compressive and tensile strengths.

The concrete characteristics were measured on six cylindrical samples 220 mm long and 110 mm in diameter, which were subjected to unconfined compression or wedge tests. Tensile tests were also conducted for the steels. The third column of Table 1 presents the values obtained experimentally and the fourth column the mean of these values.

2.3. Numerical modeling

2.3.1. Finite element analysis

To investigate the mechanical response of the structure and to take into account the nonlinear properties of the materials, the RC wall was modeled based on the FEM (Finite Element Method) to solve the equation of motion, which can be written as:

$$M\ u(t) + C\ \dot{u}(t) + F_{int}(u(t), \dot{u}(t)) \qquad F_{ext}(t) \tag{1}$$

where M is the mass matrix, C the damping matrix, F_{int} the internal resisting forces, F_{ext} the force applied on the structure and u is the unknown displacement field.

To solve the problem, the finite element code Cast3M (Millard, 1993) was chosen.

The transient loading is taken into account using the step by step procedure, which involves a Newmark implicit time stepping method (average acceleration time integration schema) and the convergence Newton Raphson method.

To reduce the CPU time, the RC structure is modeled in two dimensions using QUA4 finite elements (quadrilateral elements comprising four nodes with a linear shape function) to discretize the concrete and SEG2 elements (linear elements comprising two nodes) for the steel.

The meshes of concrete and steel that constitute the 1/6 scale and full scale structures are presented in Fig. 6.

For concrete, every element measures approximately 3 cm by 3 cm for the small scale model, resulting in 53 elements in height and 34 elements in width, of a total of 632 elements and 18 cm by 18 cm for the full scale model of a total of 1077 elements.

A perfect bond between concrete and steel was assumed, which means that no sliding between concrete and steel rebars is taken into account and the strains of both materials are similar at the interface.

The characteristics of the steel rebars and the reinforcement ratio introduced in the numerical model are presented in Table 2 for the 1/6 scale model and in Table 3 for the full scale structure. To take into account the spatial distribution in 3D, the reinforcement ratio introduced in the numerical model (column 7) for each type of rebar (column 4) was taken equal to the actual section of rebar (column 6) multiplied by the number of such rebars in the length L of the structure (column 5) and divided by this length.

Table 1
Geometry and mechanical properties of the structure in the 1/6 and full scales.

Parameter	Symbol	Experimental values	Mean	Calibration value	Unit
Vertical wall geometry					
Height	h	1.60 or 9.60	–	–	m
Thickness	e_p	0.25 or 1.50	–	–	m
Length	L	2.50 or 14.80	–	–	m
Base geometry					
Width	l	1.00 or 9.00	–	–	m
Thickness	e_p	0.25 or 1.50	–	–	m
Length	L	2.50 or 14.80	–	–	m
Concrete properties					
Density	ρ^c	–	–	2500	kg/m^3
Young's modulus	E_y^c	38,842 and 38,925	38,884	38,840	MPa
Poisson's ratio	ν^c	0.18 and 0.3	0.24	0.2	–
Compressive strength	f_c^c	76; 77.4; 77.9 and 78.3	77.4	80	MPa
Tensile strength	f_t^c	6.5 and 6.8	6.65	5.5	MPa
Steel properties					
Density	ρ^s	–	–	7500	kg/m^3
Young's modulus	E_y^s	–	217,000	217,000	MPa
Poisson's ratio	ν^s	–	0.3	0.3	–
Yield strength	f_y^s	–	575	400	MPa
Ultimate tensile strength	f_u^s	–	620	445	MPa
Ultimate strain	ε_u^s	–	0.037	0.037	–

Table 2
Geometry properties of the steel rebars in the 1/6-scale structure.

Name	Abscissa x	Ordinate y	Type	Number	Section in m^2	Ratio in m^2/m
LA1	0.03	From 1.36 to 1.57	HA10	21	1.6493×10^{-3}	6.597×10^{-4}
LA2	0.03	From 0.36 to 1.36	HA10	42	3.2987×10^{-3}	1.3195×10^{-3}
LA3	0.03	From 0.25 to 0.36	HA10	21	1.6493×10^{-3}	6.597×10^{-4}
LA4	0.06	From 0.59 to 0.71	HA12	21	2.3750×10^{-3}	9.500×10^{-4}
LA5	0.06	From 0.30 to 0.59	HA12	42	4.7501×10^{-3}	1.9000×10^{-3}
LA6	0.06	From 0.03 to 0.30	HA12	63	7.1251×10^{-3}	2.8501×10^{-3}
LA7	From 0.06 to 0.97	0.03	HA12	63	7.1251×10^{-3}	2.8501×10^{-3}
LA8	From 0.03 to 0.97	0.22	HA6	14	3.958×10^{-4}	1.583×10^{-4}
LA9	0.22	From 0.03 to 0.25	HA8	10	5.027×10^{-4}	2.011×10^{-4}
LA10	0.22	From 0.25 to 0.48	HA8	20	1.0053×10^{-3}	4.021×10^{-4}
LA11	0.22	From 0.49 to 1.57	HA8	10	5.027×10^{-4}	2.011×10^{-4}

Table 3
Geometry properties of the steel rebars in the full-scale structure.

Name	Abscissa x	Ordinate y	Type	Number	Section in m^2	Ratio in m^2/m
LA1	0.03	From 8.16 to 9.57	HA25	98	4.8106×10^{-2}	3.2504×10^{-3}
LA2	0.03	From 2.16 to 8.16	HA25	196	9.6211×10^{-2}	6.5008×10^{-3}
LA3	0.03	From 1.50 to 2.16	HA25	98	4.8106×10^{-2}	3.2504×10^{-3}
LA4	0.06	From 3.55 to 4.26	HA32	100	8.0425×10^{-2}	5.4341×10^{-3}
LA5	0.06	From 1.82 to 3.55	HA32	200	1.60850×10^{-1}	1.08682×10^{-2}
LA6	0.06	From 0.03 to 1.82	HA32	300	2.41274×10^{-1}	1.63023×10^{-2}
LA7	From 0.06 to 8.97	0.03	HA32	300	2.41274×10^{-1}	1.63023×10^{-2}
LA8	From 0.03 to 8.97	1.47	HA14	76	1.1699×10^{-2}	0.7905×10^{-3}
LA9	1.47	From 0.03 to 1.50	HA14	98	1.5086×10^{-2}	1.0193×10^{-3}
LA10	1.47	From 1.50 to 2.88	HA14	196	3.0172×10^{-2}	2.0386×10^{-3}
LA11	1.47	From 2.88 to 9.57	HA14	98	1.5086×10^{-2}	1.0193×10^{-3}

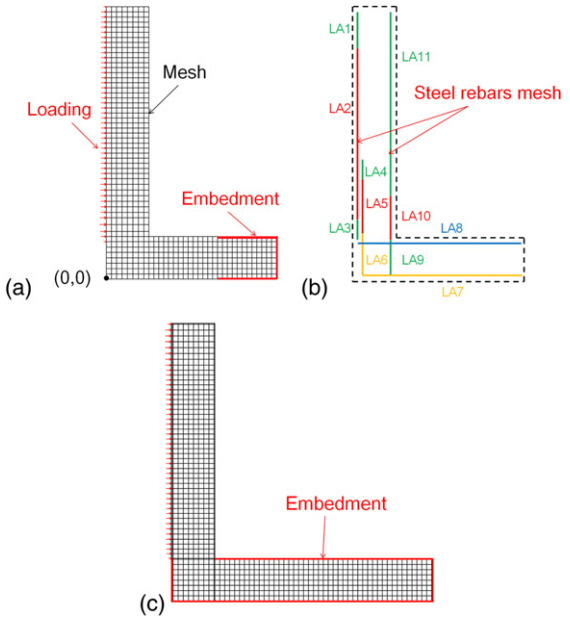

Fig. 6. (a) Boundary conditions and mesh of concrete in the small-scale model, (b) mesh of steel of the small-scale model and (c) boundary conditions of the full-scale model.

According to the experimental conditions, the base of the 1/6 scale structure is clamped over 35% of the base length between 0.65 and 1 m (Figs. 3a and 6a). No displacement and no rotation can occur in this part of the structure. Meanwhile, the base of the full scale model was assumed to be completely embedded (Figs. 3b and 6c).

2.3.2. Applied loading

A uniform pressure field is applied over the total height of the face exposed to the snow avalanche (Fig. 6a). The applied pressure is assumed to be constant along the vertical direction. The weight of the structure (36 kN for the 1/6 scale model and 9310 kN for the full scale model) is also taken into account. Indeed, it is insignificant compared to the ultimate pressure applied (350 kPa, which corresponds to 1210 kN for the 1/6 scale model and to 41,960 kN for the full scale model) except for the beginning of the loading.

2.3.2.1. Pushover tests

To calibrate the numerical model on the experimental test presented above, a pushover loading is simulated on the 1/6 scale model. A pushover test consists in a quasi static test with a linear increase in the loading until the structural collapse. The applied loading is chosen according to the experimental pushover test performed on the physical model. In this case, the loading varies linearly from 0 to 350 kPa, as illustrated in Fig. 7.

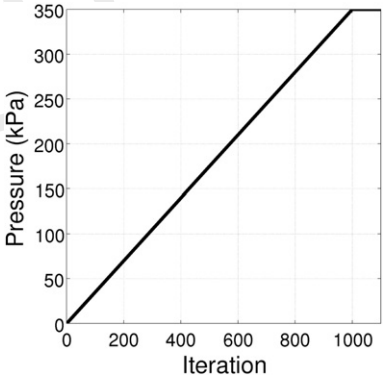

Fig. 7. Pressure profile applied to the upstream face of the structure in pushover tests.

Moreover, the calculation is conducted under quasi static conditions (Eq. (1) reduced to $F_{int} = F_{ext}$).

2.3.2.2. Avalanche signals

In mountainous areas, three types of snow avalanches are generally considered. Dense snow avalanches have a high density (varying between 100 and 500 kg/m^3), whereas powder avalanches have a low density (lower than 20 kg/m^3). Between the two, mixed avalanches are composed of a dense layer flowing at the bottom, combined with a powder snow cloud on top. The average pressure applied on a structure by such flows is defined as follows: $P \quad \frac{1}{2} C_d \rho v^2$ where ρ and v are respectively the density and the velocity of the avalanche. The drag coefficient $C_d = C_r C_o$ depends on the avalanche flow regime (C_r, equal to 1 for powder snow avalanches and able to reach values of 15 30 for dense snow avalanches) and the obstacle geometry (C_o) (Salm et al., 1990).

In the present case, the studied structure is located on the Taconnaz avalanche path, where several large dense and mixed avalanches occurred during the last century, down to the runout area where the defense structure has been set up. In this location, the velocity of the dense part of the snow avalanche (v_d) is around 40 m/s and its density (ρ_d) varies from 250 kg/m^3 to 500 kg/m^3 according to the snow quality and the involvement of ice, which can represent 30% of the volume. The velocity magnitude of the powder part (v_p) is around 40 50 m/s and its density (ρ_p) can be estimated at 10 kg/m^3. Consequently, the ratio of pressures developed by the dense and powder parts $\left(\frac{\rho_d v_d^2}{\rho_p v_p^2}\right)$ is around 20. Because dense flows generate the most significant destructive forces, only dense snow avalanches will be studied in the following. Furthermore, the back analysis of 49 events carried out by Naaïm et al. (2010), showed that the height of the dense snow avalanche at the entrance of the stopping zone is between 6 and 10 m.

Here, two types of avalanche pressure profiles, presented in Fig. 8a, are tested. The first one is a synthetic triangular shaped signal inferred from typical pressure signals reported in Thibert et al. (2008) and Baroudi and Thibert (2009). The other one has the shape of an actual avalanche signal measured in situ on the Irstea experimental test site located at the Lautaret pass in the French Alps (Thibert et al., 2008). This last signal is also typical of a dense snow avalanche, with a peak pressure at the avalanche head, a plateau pressure at the core of the avalanche, and a pressure discharge at the avalanche tail. The time histories of the synthetic and measured signals are plotted in Fig. 8b.

As specified in Fig. 8, the two types of signals are described by the pressure at peak P_{max} and the rise time t_m, which is defined as the time needed to reach the maximum pressure during the loading. The loading time is then equal to:

$$t_l \quad 2\,t_m \tag{2}$$

in the case of the synthetic triangular signal, or

$$t_l \quad \frac{16}{3.5}\,t_m \tag{3}$$

in the case of the avalanche signal as in Lautaret. t_{end} corresponds to the end of the simulation and is at least equal to 2 t_l, to obtain the essential of the structural response.

Numerical simulations are carried out under dynamic conditions where damping is defined from the Rayleigh approach such as:

$$C \quad \alpha M + \beta K \tag{4}$$

where α and β are the Rayleigh coefficients, which are calculated from the natural pulsations of the wall $\omega_1 = 2\,\pi\,f_1$ and $\omega_2 = 2\,\pi\,f_2$ and by damping ratios ξ_1 and ξ_2: $\alpha \quad \frac{2\,\omega_1\,\omega_2\,(\xi_1\,\omega_1 \quad \xi_2\,\omega_2)}{\omega_1^2 \quad \omega_2^2}$ and $\beta \quad \frac{2\,(\xi_1\,\omega_1 \quad \xi_2\,\omega_2)}{\omega_1^2 \quad \omega_2^2}$.

Damping ratios here equal to $\xi_1 = \xi_2 = \xi = 5\,\%$ (the value usually used in seismic engineering (Brun, 2002; Brun et al., 2003; Pecker, 2010)).

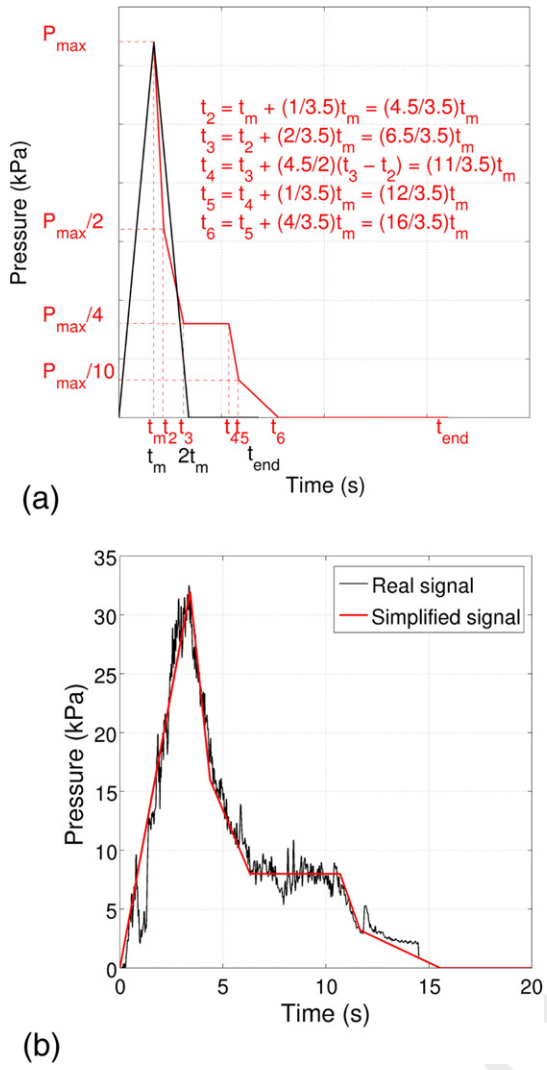

Fig. 8. a) Two types of avalanche signals introduced in the model of the actual-scale structure: in black, the synthetic isosceles triangular signal and in red, the synthetic avalanche signal, compared in b) with the full-scale signal measured in situ at the Lautaret pass in the French Alps (Thibert et al., 2008).

2.3.3. Constitutive laws

2.3.3.1. Concrete descriptions

For model calibration purposes, four nonlinear constitutive laws were tested to describe the concrete mechanical behavior.

- Standard elasto plastic law (CEA concrete model)
  The first model is a simple elasto plastic model proposed by the French CEA research center, first developed by Nahas (1986) and then modified by Leprêtre et al. (1988). It describes uniaxial tensile and compressive behaviors of concrete with linear stress strain relationships (Fig. 9b).
  When concrete is uncracked, the classical plasticity theory based on the smeared fixed crack approach is used. Concrete cracking is governed by the maximum tensile stress criterion (Fig. 9a). Then, when the crack detection surface is reached in tension, a virtual crack is created perpendicular to the principal stress direction and its direction is kept constant until the end of the simulation. A second crack can appear only in the perpendicular direction. A negative hardening in compression is initiated when a Drucker Prager criterion is reached (Fig. 9a).
  Finally, the concrete model is defined by nine parameters: the density of concrete ρ^c, two elastic parameters E_y^c and ν^c, the uniaxial and biaxial compressive strengths f_c^c and $f_{cc}^c = 1.16\, f_c^c$, the tensile strength f_t^c, the ultimate strains in compression and tension ε_{uc}^c and ε_{ut}^c and a reduction coefficient of shear modulus in case of cracking *Betr*, between 0 and 1 (by default equal to 0.1).

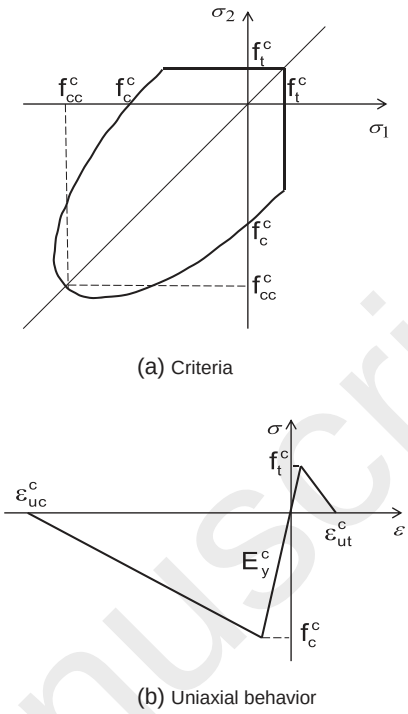

Fig. 9. CEA concrete model: (a) yield criteria and (b) uniaxial behavior.

- Cyclic elasto plastic law (INSA concrete model)
  This concrete constitutive law was developed at INSA in Lyons (Merabet, 1990) and has been used in the last decade for engineering structures subjected to seismic loading (Brun et al., 2003; Ile and Reynouard, 2000, 2005). Two laws for the concrete modeling can be distinguished, depending on whether the concrete is cracked or uncracked. It differs from the first elasto plastic constitutive law described in this paper in the shape and the evolution rule of the yield surfaces, which here follow the Nadaï criteria (of the Drucker Prager type), a positive isotropic hardening before reaching the ultimate yield in compression, and it can take into account a cyclic loading.
  The INSA model is defined by eight parameters: the density of concrete ρ^c, two elastic parameters E_y^c and ν^c, the compressive and tensile strengths f_c^c and f_t^c, the ultimate strains in compression and tension ϵ_{uc}^c and ϵ_{ut}^c, and a transfer factor of shear *Ftc* (by default equal to 0.4).

- Standard damage model (Mazars concrete model)
  The third law tested on concrete is the elastic damage model developed by Mazars (1986), where the influence of microcracking is introduced via a single scalar damage variable D ranging from 0 (for undamaged material) to 1 (for completely damaged material).
  This variable is described by a damage threshold ϵ_{d0} and four material parameters, A_c, A_t, B_c and B_t, which are used to calibrate the shape of the curves. They describe the assumptions of the post peak stress strain curves in compression and in tension, at the end and at the beginning, respectively.
  These parameters were not experimentally identified. Thus the following empirical relationships, implemented in Cast3M, were used to determine their respective values:

$$\epsilon_{d0} \quad \frac{f_t^c}{E_y^c} \tag{5}$$

$$A_t \quad 1-\frac{f_{tr}^c}{f_t^c} \tag{6}$$

where f_{tr}^c is the residual tensile strength. The tensile asymptotic stress f_{tr}^c / f_t^c generally equals 0; in that case, $A_t = 1$.

$$B_t \quad \frac{1+I_f^c}{\epsilon_{d0}} \tag{7}$$

B_t is generally equal to $\frac{1}{\epsilon_{d0}}$ but can be compensated by a tensile brittle ness index I_f^c, equal to 0 for a perfect yield material and to 1 for a very brittle material.
The values A_c and B_c are obtained by deriving the compressive uniax ial law and identifying the minimal stress with the corresponding strain:

$$A_c \quad \frac{\epsilon_{d0} - \quad 2^{0.5}\,|f_c^c|\,\frac{\nu^c}{E_y^c}\Big)\Big)\,B_c}{B_c\,\epsilon_{d0} - exp\,(B_c\,\epsilon_{d0} - 1)} \tag{8}$$

$$B_c \quad \frac{1}{2^{0.5}\,\nu^c\,|\epsilon_c^c|} \tag{9}$$

where ϵ_c^c is the strain corresponding to f_c^c and here equals $3\,f_c^c / E_y^c$.
To summarize, the Mazars model is described by eight parameters: the density of concrete ρ^c, two elastic parameters E_y^c and ν^c, the compres sive and tensile strengths f_c^c and f_t^c, the residual tensile strength f_{tr}^c, the tensile brittleness index I_f^c and a correction factor *Beta* for shear (whose recommended value equals 1.6, giving a better convergence of the model).

- Damage and sliding model (Ricrag concrete model)
  The Ricrag model was developed by Richard (2010b) to describe the behavior of concrete under seismic loadings. It is a model combining elasticity, isotropic damage and internal sliding.
  The damage mechanism is accounted for by decreasing Young's modulus of the material and can represent the stiffness reduction due to concrete cracking. Damage occurs when the initial energy damage threshold Y_0 is reached. Y_0 can be linked to the tensile strength through the relation $Y_0 \quad \frac{(f_t^c)^2}{2\,E_y^c}$, (Adélaïde et al., 2012; Richard, 2010a), used by Cast3M. Then the damage mechanism under tensile and compressive regimes is described by brittleness in tensile and compression. More over, crack friction can occur and lead to energy dissipation. Under cy clic loadings, the frictional sliding is described by a hysteretic behavior involving isotropic and kinematic work hardening. The nonlinear hardening modulus a_0 can control the nonlinearity of the transition between the secant and elastic moduli during an unloading phase, whereas the kinematic hardening modulus γ_0 allows acting on the size of the hysteresis loops.
  To summarize, the Ricrag model is described by eight parameters: the density of concrete ρ^c, two elastic parameters E_y^c and ν^c, the tensile strength f_t^c, the brittleness in tension and compression A_{Dir} and A_{Ind}, and two hardening moduli a_0 (nonlinear hardening) and γ_0 (kinematic hardening).

2.3.3.2. Steel

A typical stress strain curve for steel consists of a linear elastic por tion, followed by the bars yielding with a weak strain hardening. The constitutive law used corresponds to the measurements obtained dur ing the experimental tests (Fig. 10) and is described by four parameters: Young's modulus E_y^s, the yield and ultimate strengths f_y^s and f_u^s, and the ultimate strain of steel ϵ_u^s. The hardening modulus (E_h^s) corresponds to the slope of the hardening curve.

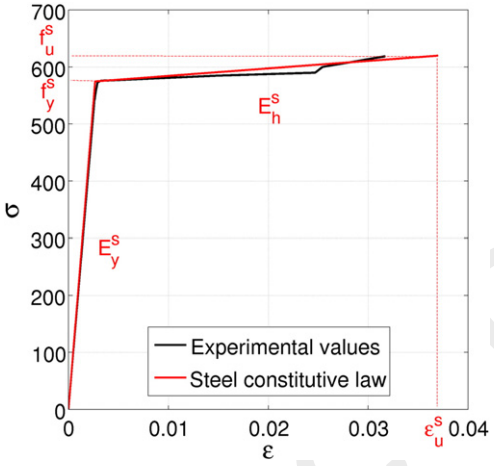

Fig. 10. Steel constitutive law.

3. FE model static calibration

3.1. CEA concrete model

The CEA numerical model was calibrated to obtain results close to those of the experimental test presented in Fig. 5b. The dimensions taken into account are those of the 1/6 scale model presented in Fig. 3a and Table 1. The applied load is that described in Fig. 7, with a loading step Δp of 350 Pa.

3.1.1. Parametric analysis

All the parameters used in the concrete constitutive law were studied in the following order: ν_c, E_c, f_t^c and f_c^c. At the beginning, each parameter was equal to the mean experimental value presented in Table 1, column 4: $E_y^c = 38,884$ MPa, $\nu^c = 0.24$, $f_c^c = 77.4$ MPa and $f_t^c = 6.65$ MPa. Moreover, tensile and compressive ultimate strains are defined by $\epsilon_{ut}^c = 3\,f_t^c / E_y^c$ and $\epsilon_{uc}^c = 10\,f_c^c / E_y^c$, respectively. For steel, the results of the tensile tests presented in Table 1, column 4 were used.

No influence of Poisson's ratio was observed on the response of the structure. Therefore, this parameter was set to the usual value of 0.2. Fig. 11a shows that concrete Young's modulus can have a substantial influence on the structural behavior, not only in the elastic domain but also after the concrete cracks. Young's modulus was set equal to 38,840 MPa (the lowest experimental value of Young's modulus), in order to correctly describe the structural elastic behavior. Fig. 11b shows that the beginning of cracking observed during the experimental tests is obtained, in numerical conditions, with a tensile strength value of 5.5 MPa, which is lower than the experimental value. The compres sive strength has an influence only on the collapse of the structure (Fig. 11c). In the following, f_c^c is equal to 78 MPa. Finally, by varying only the concrete parameters, the final result shown in Fig. 11c does not agree with the experimental strength displacement curve, espe cially when rebar yielding occurs. Therefore, a parametric study on the steel characteristics was also conducted.

As Mirza and MacGregor (1979) and noted, Young's modulus of steel has a small dispersion. Therefore, the influence of this parameter is not described here and the experimental value is retained. Fig. 11d displays the influence of the steel yield limit, keeping the ultimate strength constant and equal to 620 MPa. The value of the steel yield limit equal to 350 MPa makes it possible to obtain the yielding of steel rebars at the same experimental loading. Nevertheless, this value is much lower than the experimental value. Then, in order to obtain the collapse of the structure for the same experimental loading, the ultimate strength (f_u^s) was varied as shown in Fig. 11e. The influence of both yield (f_y^s) and ultimate (f_u^s) limits was studied (Fig. 11f). E_h^s is assumed to be

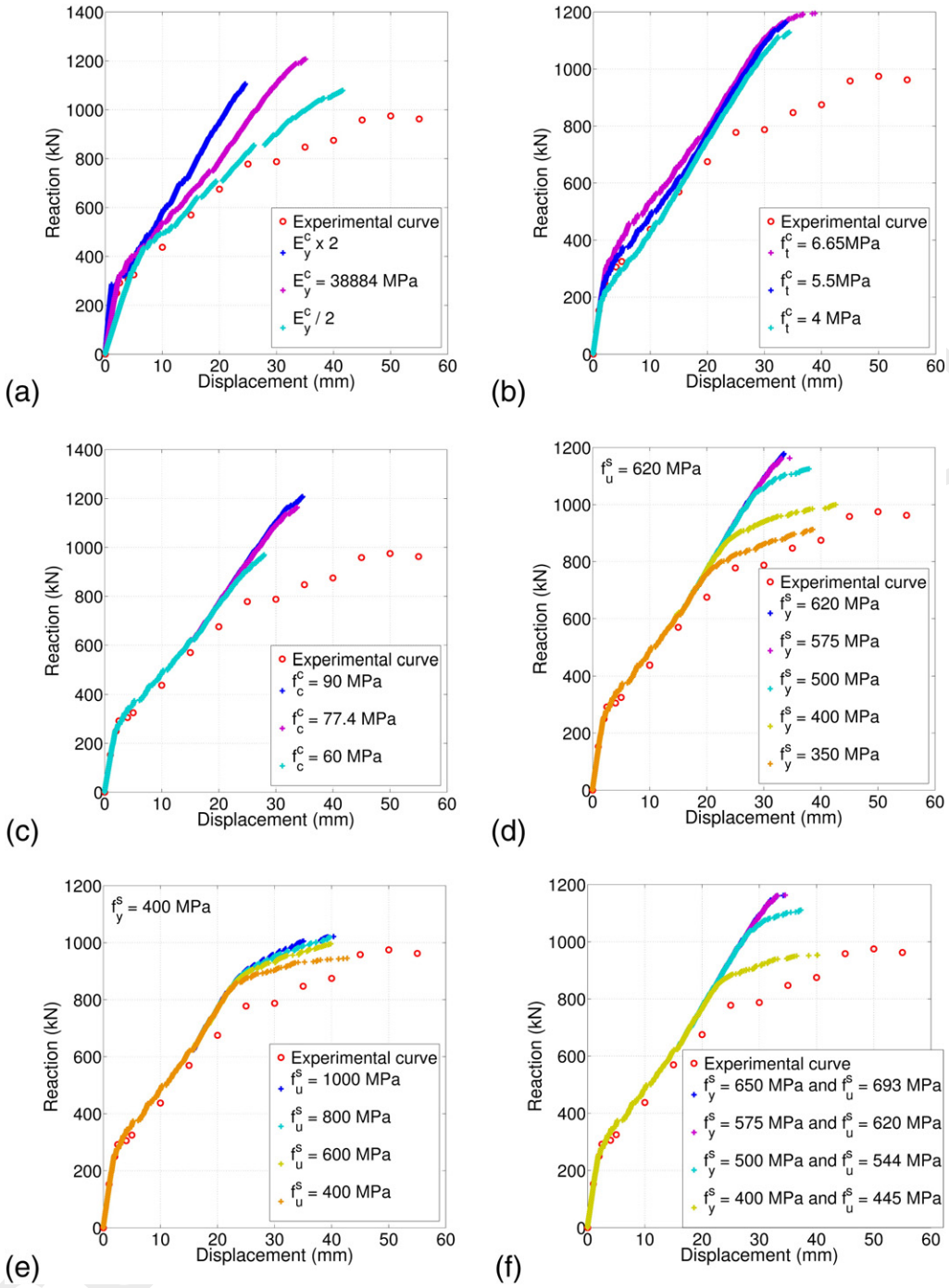

Fig. 11. CEA concrete model: Influence of different materials characteristics on the response of the structure: (a) Young's modulus of concrete, (b) the tensile and (c) compressive strengths of concrete, (d) the yield and (e) ultimate limits of steel and (f) combined yield and ultimate limits of steel, the hardening ratio remaining constant.

constant and equal to the experimental value of 1310 MPa. Finally, the best result is obtained for $f_y^s = 400$ MPa and $f_u^s = 445$ MPa.

3.1.2. RC structure model calibration

The parametric study on the materials characteristics highlights the influence of the different materials parameters on the structural mechanical response (Fig. 12).

The first part of the structure response is totally elastic and controlled by concrete Young's modulus. Then the concrete begins to crack when the tensile strength of concrete is reached and the rebars remain elastic. Indeed, the structural response is controlled by steel Young's modulus. Next, rebar yielding begins and the curve slope is equal to steel hardening modulus. Finally, the collapse is obtained when the ultimate tensile strength of steel is reached.

All the values introduced in the numerical model after calibration are indicated in the fifth column of Table 1. Moreover, the reduction coefficient of shear modulus equals 0.1. To obtain an accurate calibration, the tensile strength of concrete was set equal to 5.5 MPa (mean experimental value: 6.65 MPa) and steel characteristics were decreased (Fig. 13). Finally, the compressive strength is equal to 80 MPa (mean experimental value: 77.4 MPa), in order to obtain the collapse for the same pressure value as the experimental value.

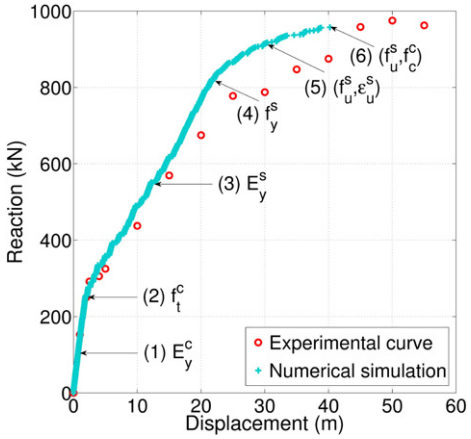

Fig. 12. CEA concrete model: Parameters that influence the different damage levels.

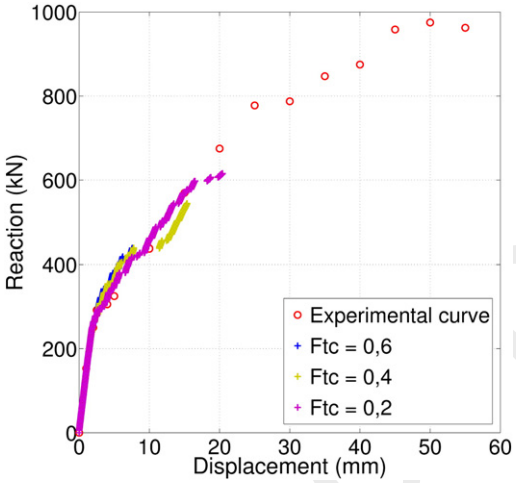

Fig. 14. INSA concrete model: Influence of the shear coefficient on the response of the structure.

3.2. INSA concrete model

The INSA and CEA models involve almost the same input parameters. Consequently, for both models, the calibration of the numerical small scale model used the same parameter values. Only an additional parame ter appears in the INSA model: the shear coefficient. The influence of this parameter is plotted in Fig. 14. The best result was obtained with a shear coefficient of 0.2 and a loading step Δp of 35 Pa.

3.3. Mazars and Ricrag concrete models

These models were calibrated at two scales. First, they were cali brated at the finite element scale to ensure that all calibrated models lead to the same effects at the element scale for uniaxial tension and compression tests. Then a last calibration associated to shear coeffi cient and loading step was carried out at the global scale in order to obtain numerical results as close as possible to the experimental results.

Thus, uniaxial tension and compression tests on a single finite element were first simulated to calibrate the Mazars and Ricrag constitutive laws. The result obtained with the CEA constitutive law is considered as the reference. A parametric study was carried out for each constitutive law (Figs. 15 and 16).

Fig. 15 shows that concrete must be considered as a rather brittle material ($I_f^c = 0.6$) with no residual tensile strength, in order to obtain good agreement with the CEA and Mazars models. The shear coefficient introduced in the Mazars model was also studied, but it had no influ ence on the response of the structure. Therefore, its value was taken equal to the default value.

Fig. 16 shows the calibration of the Ricrag model, so that a result close to CEA model was obtained.

First, the nonlinear and kinematic hardening moduli were taken as equal to the values recommended by Richard (2010a): respectively, 7×10^{-7} Pa^{-1} and 7×10^{9} Pa. Indeed, the author recommends that these values not be modified too much to avoid a divergence of the in tegration algorithm. Moreover, the first values of the concrete brittle ness are also equal to the values retained by Richard (2010a): 1×10^{-2} J^{-1} m^3 in tension and 8×10^{-5} J^{-1} m^3 in compression. Given that the results are far from those obtained with the CEA model, the values of a few parameters were modified, but the 7×10^{7} Pa value retained for the kinematic hardening modulus quickly leads to a divergence in the case of the L shaped wall (Fig. 18).

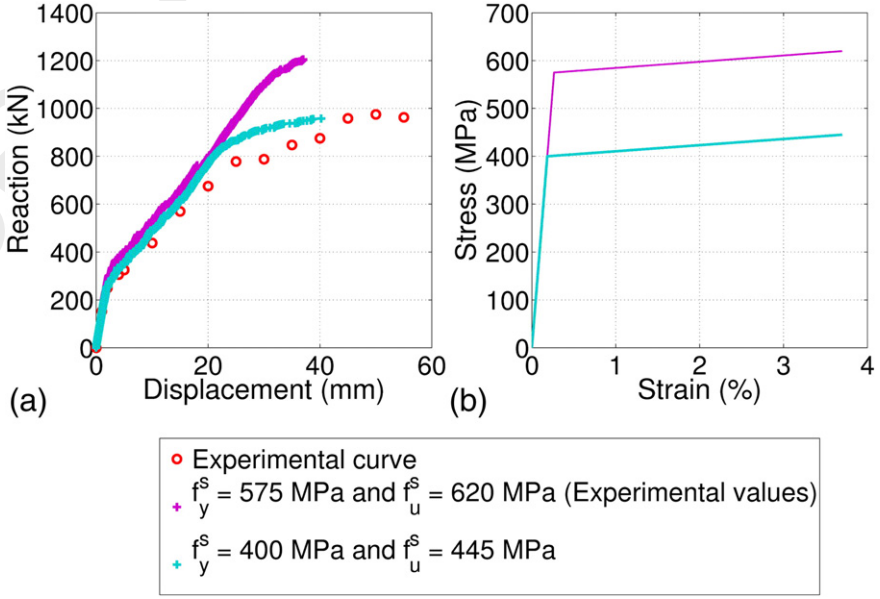

Fig. 13. CEA concrete model: Comparison of (a) the structure responses and (b) the steel constitutive laws before and after calibration.

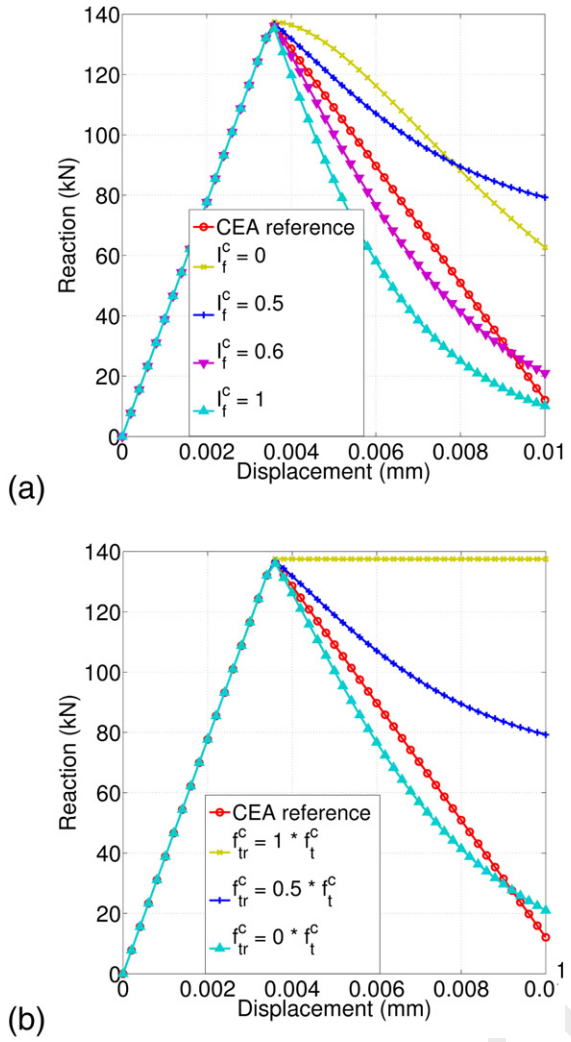

Fig. 15. Mazars concrete model: Influence of (a) the brittleness index (I_f^c) and (b) the residual tensile strength (f_{tr}^c) of concrete on the response of a single finite element under a uniaxial tension loading.

Finally, Fig. 17 shows the uniaxial behavior in compression and tension for each constitutive law after calibration. Good agreement with the different constitutive laws was obtained.

The values retained after calibration for the specific parameters of each law are presented in Table 4.

3.4. Force displacement curves

At the scale of the L shaped wall, force displacement curves for the different constitutive laws are plotted in Fig. 18. Only the two Mazars and CEA models obtain the ultimate force before structural collapse. For the INSA and Ricrag models, the algorithm diverges very quickly after the nonlinearities appear and are not able to describe rebar yielding.

Concerning the Mazars model, in order to improve the result accuracy and to facilitate the code convergence, the loading step was divided by 10 (equal to 35 Pa), which led to a considerable increase in the CPU time. Nevertheless, this model still presents some convergence problems.

Solutions such as the decrease of calculation precision and a calculation under dynamic conditions with a little damping were tested to obtain better results with the INSA and Ricrag models. None of these attempts improved the results.

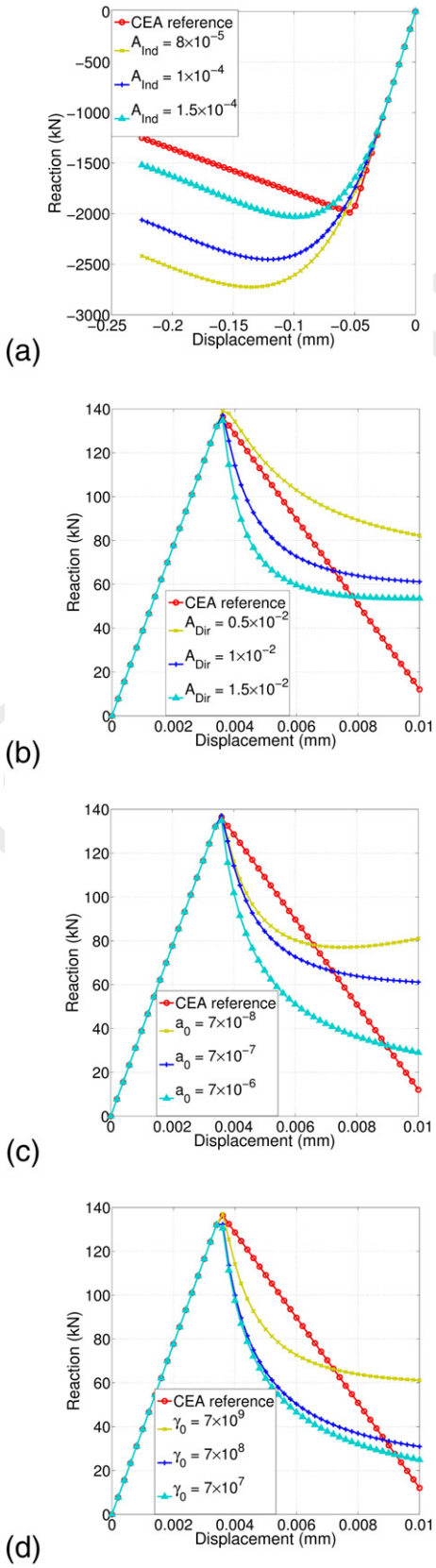

Fig. 16. Ricrag concrete model: Influence of brittleness in (a) compression and (b) tension and the (c) nonlinear and (d) kinematic hardening in tension on the response of a single finite element.

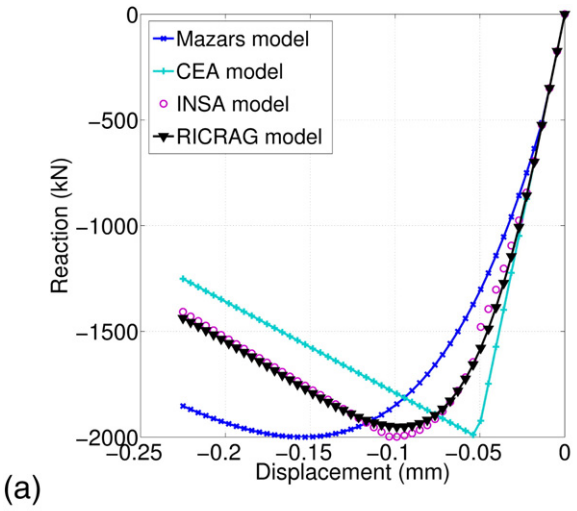

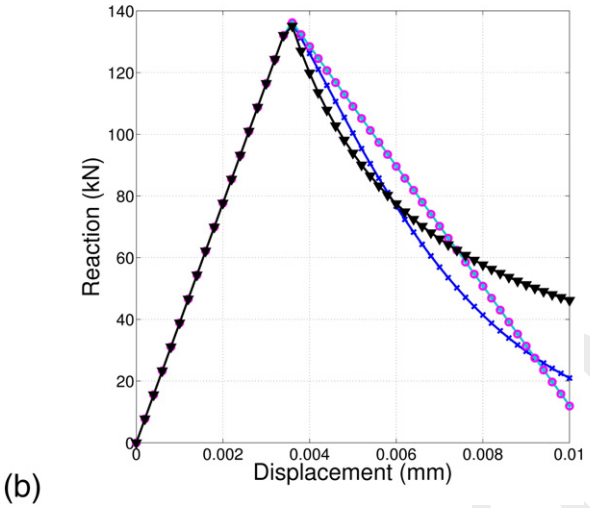

Fig. 17. Calibration results of the four constitutive laws tested for (a) compressive and (b) tensile uniaxial load applied to a single finite element.

3.5. Failure mode

Fig. 19 presents the values of the scalar damage variable (D) for the Mazars and Ricrag models, the values of the damage in direction 1 ($DAM1$) for the CEA model and the values of a cracking state indicator

Table 4
Calibration parameters of the different constitutive laws.

Constitutive law	Parameter	Symbol	Retained value	Unit
CEA	Reduction coefficient of shear modulus	$Betr$	0.1	–
	Loading step	Δp	350	Pa
Mazars	Residual tensile strength	f_{tr}^{c}	0	MPa
	Brittleness index	I_f^c	0.6	–
	These values lead to $\varepsilon_{d0} = 1.4 \times 10^{-4}$, $A_t = 1$, $B_t = 11$, 300, $A_c = 0.8$, and $B_c = 570$.			
	Shear coefficient	$Beta$	1.6	–
	Loading step	Δp	35	Pa
INSA	Shear transfer factor	Ftc	0.2	–
	Loading step	Δp	35	Pa
Ricrag	Brittleness in tension	A_{Dir}	0.5×10^{-2}	J^{-1} m^3
	Brittleness in compression	A_{Ind}	1.5×10^{-4}	J^{-1} m^3
	Nonlinear hardening	a_0	7×10^{-7}	Pa^{-1}
	Kinematic hardening	γ_0	7×10^{7}	Pa
	Loading step	Δp	35	Pa

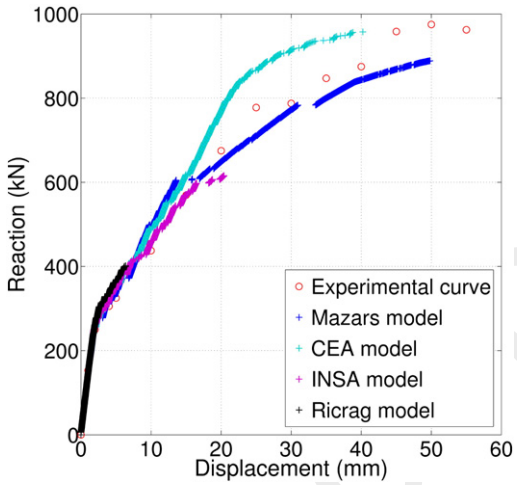

Fig. 18. Structure response after calibration for the four constitutive laws.

(*JFIS*), equal to 1 when the cracking is initialized and 0 in the opposite case for the INSA model.

The first cracks were correctly obtained for the four models (Fig. 19b, d, f and g) but at lower pressures than in experimental conditions. Indeed, in the four numerical models, the first cracks appear at 50 kPa in the base and 80 kPa in the vertical wall. Meanwhile, Fig. 19c and e, describing the collapse at the last converging step for the two converging models, show that only the Mazars model seems to represent accurately the ultimate macro crack, which leads to the collapse of the structure.

For the CEA model, at the onset of cracking, the crack distribution matches that observed in the experimental case; but in the end, the inclined crack, which is characteristic of shear failure, is not clearly represented.

In contrast, for the Mazars model, the inclined crack seems to be correctly predicted and accurately located.

3.6. Discussion

To obtain good agreement with the numerical and experimental results in quasi static conditions, the tensile strength of concrete was not taken to be equal to the experimental value (6.65 MPa). The value retained (5.5 MPa) was far from the experimental value obtained by tensile tests. Nevertheless, it corresponds to the value that can be calculated from concrete compressive strength according to the formula:

$$0.3 f_c^{c\,2/3} \tag{10}$$

as recommended in codes such as Eurocode 2 part 1 1 (CEN, 2005). Moreover, concrete is generally used for its compressive features and its tensile strength is often neglected in design.

Furthermore, steel strengths were decreased. The hypothesis of a perfect bond between concrete and steel can explain the need to decrease the values of the yield and ultimate strengths of steel. Indeed, the rebar surface in contact with concrete is greater than in reality and leads to stresses underestimating within steel. To obtain the yielding beginning and the failure of the steel rebars for the same experimental loading pressure, it was necessary to decrease the strength of steel. Thus, the hardening modulus E_h^s was kept equal to the experimental modulus and the ultimate strength was calculated according to:

$$f_u^s \quad f_y^s + E_h^s \quad \epsilon_u^s - \frac{f_y^s}{E_y^s}\Big). \tag{11}$$

To explain the reduction in steel strength to account for the effect of the bond between steel and concrete on the overall structural response,

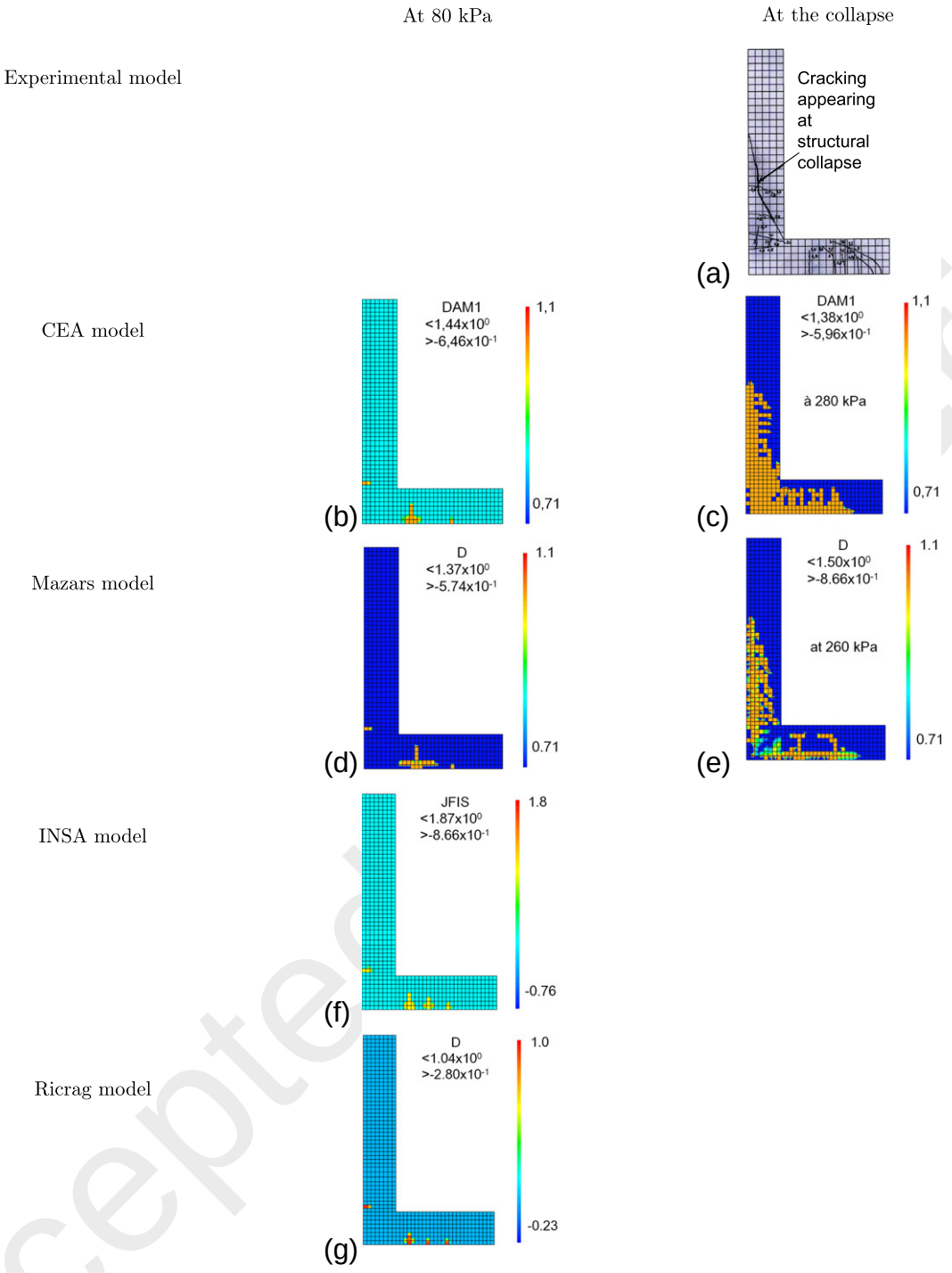

Fig. 19. Cracking observed (a) experimentally and (b), (c), (d), (e), (f) and (g) with the numerical models at 80 kPa and the last converging step.

a cantilever beam was simulated (Fig. 20a). A single steel rebar was placed within the tensile zone and a transversal pressure field was applied. Two approaches were used to describe the interface between steel and concrete. First, a perfect bond was assumed where no sliding could develop at the interface. Second, an elastic joint model described the potential interface sliding where a normal stiffness (k_n) and a shear stiffness ($k_s = k_n / 2.5$) were introduced. Steel and concrete behaviors were modeled by the preceding elasto plastic law and CEA model, respectively.

In Fig. 20b, force displacement curves were compared in the case of a perfect bond and an elastic joint for several steel strength values and k_n values, respectively. During the initial linear increase, which corresponds to the elastic response of the beam, the same curves were obtained. Then the development of material nonlinearities (such as the appearance of cracking) caused a substantial decrease of beam stiffness, leading to a plateau. The large increase in displacement at a constant load reflects the stress redistribution within the beam. Therefore, the steel rebar is fully active and carries a high proportion of the loading. The final force increase is related to the steel hardening. Equivalent results can be obtained for both modeling procedures, which justifies decreasing the steel yield strength to account for the effects occurring at the interface between the steel rebars and the concrete.

Finally, the previous results showed that the CEA model provides pressure and displacement values at collapse closer to the experimental

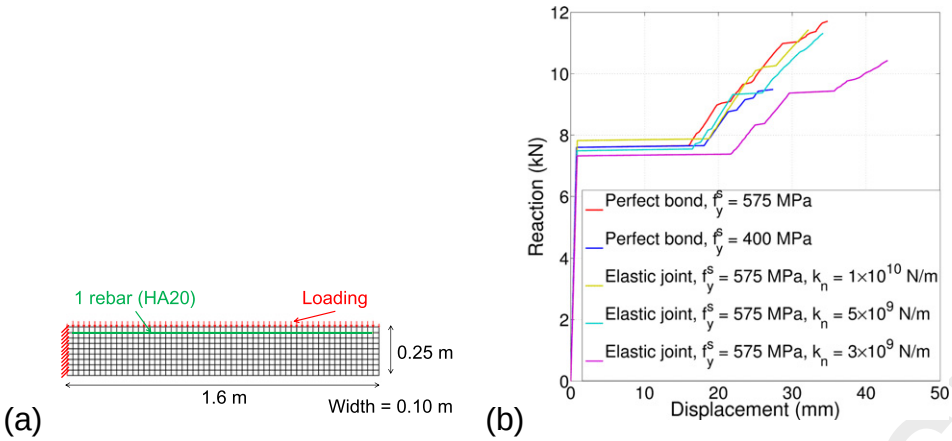

Fig. 20. (a) Beam model and (b) the influence of the bond between steel and concrete on the structural response.

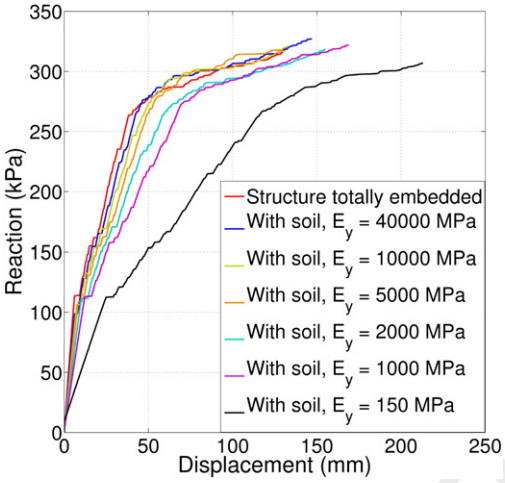

Fig. 21. Influence of the soil-structure interaction for different Young's moduli of the soil.

observations than the Mazars model, but the latter provides a better description of the failure mode. Moreover, the CPU time is much shorter for the CEA model (around 20 min) than for the Mazars model (around 2 h).

4. Full-scale protective RC structure subjected to snow avalanches

Because the objective of this study was to determine the vulnerability and the failure probability of such a structure, the carrying capacity had to be estimated and fast calculation models were required. Indeed, the vulnerability of a structure subjected to a natural hazard can be described with a damage index between 0 and 1 (0 for the undamaged structure and 1 for the structural failure), which depends on the magnitude of the natural hazard. In the case of avalanche loadings, vulnerability curves can be derived by varying the maximum pressure applied to the structure with the damage index described as a function of the deflection (Bertrand et al., 2010). Here the most important parameters are the values of pressure and deflection of the structure at failure. Furthermore, in order to perform a reliability study, the CPU time should be as low as possible. This is the reason why the CEA model was preferred for future studies.

4.1. Boundary conditions and pushover analysis

The effect of the stiffness of the boundary condition was investigated. An elastic soil meshed with three node finite elements (TRI3) was modeled. Its width on both sides of the base and its thickness under the base were set equal to the width of the structure $l = 9$ m. Several Young's moduli of the soil (E_y) were tested (from 150 to 10, 000 MPa for soils, from gravel to rock, and 40, 000 MPa, as for concrete). The results are depicted in Fig. 21. The lower the elastic modulus of the soil is, the less stiff the apparent structure is. Moreover, the stress redistribution appears earlier for the totally embedded structure than for structures modeled with a fraction of the soil. On the other hand, the failure modes and the pressures leading to the collapse of the structure are nearly the same in all different cases (Fig. 22). Finally, a total embedment was used in the following.

The quasi static reference curve of the full scale structure, obtained with a pushover test, corresponds to the red curve in Fig. 21.

4.2. Dynamic analysis

The first two natural frequencies of the structure are $f_1 = 14.5$ Hz and $f_2 = 79$ Hz. The Rayleigh coefficients equal $\alpha = 7.72$ and $\beta = 1.7 \times 10^{-4}$.

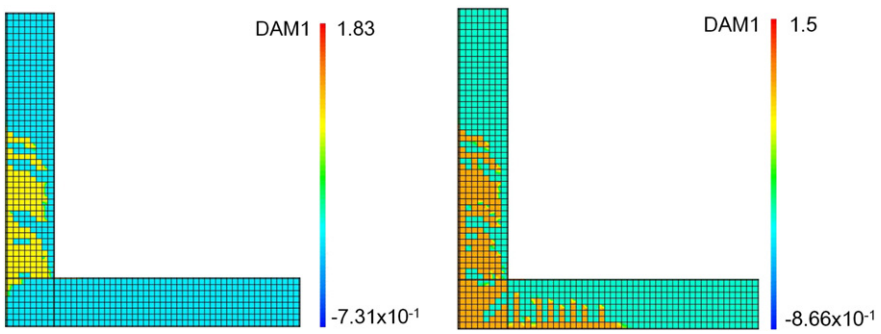

Fig. 22. Failure mode of the full-scale structure model: (a) total embedded or (b) taking into account a soil whose Young's modulus equals 150 MPa.

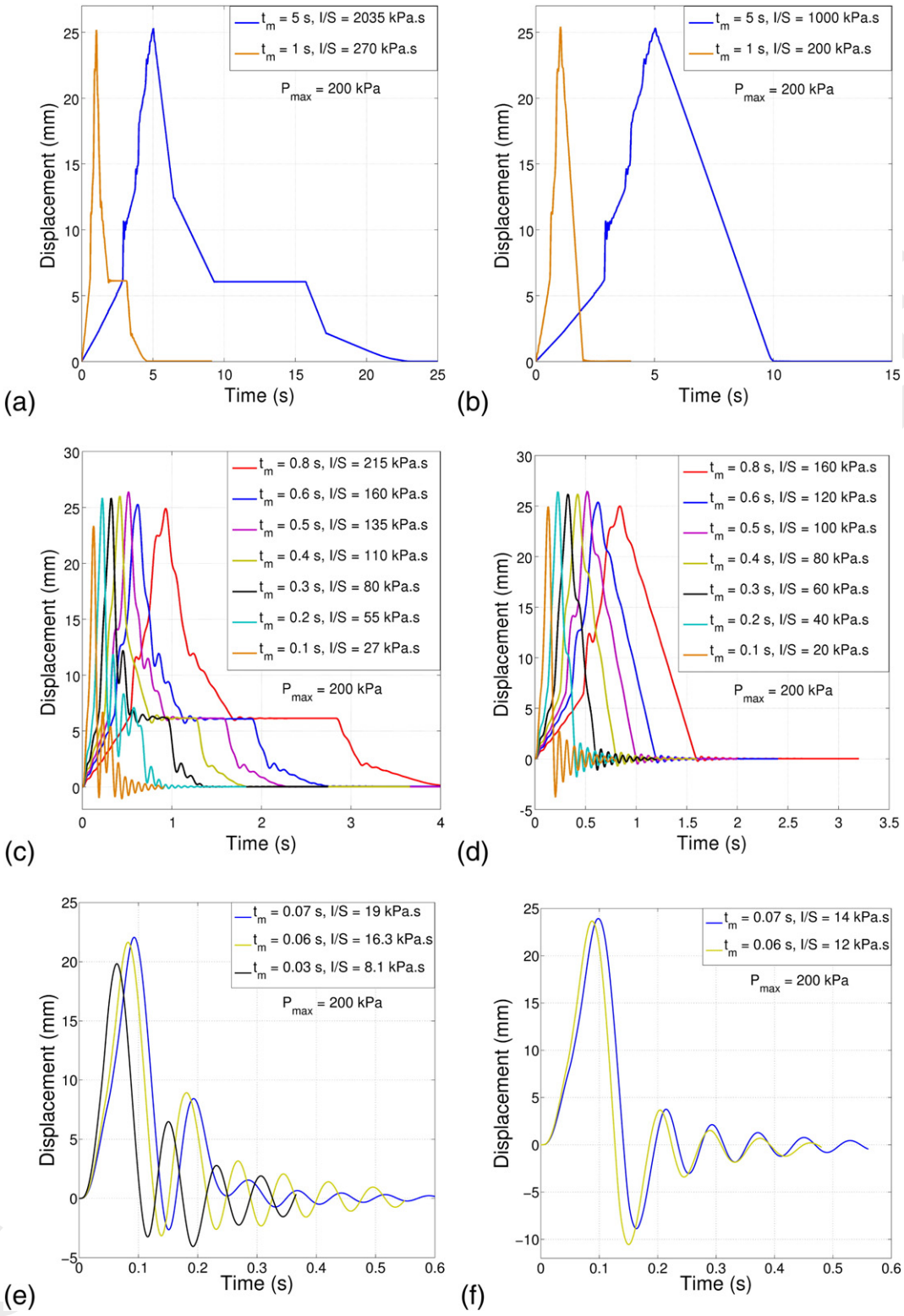

Fig. 23. Influence of the rise time and the shape of the loading signal on the structural response: (a), (c) and (e) are obtained for an avalanche signal whose maximum pressure equals 200 kPa, whereas (b), (d) and (f) are obtained for a triangular signal with a maximum pressure of 200 kPa.

Furthermore, the characteristic time of the structure response can be esti mated at $t_{str} \quad \frac{1}{f_1} \quad 0.07$ s.

Two types of avalanche signals (Fig. 8a), totally described by P_{max} and t_m, were used. The influence of the parameter t_m, for a given maxi mum impact pressure of 200 kPa and a pressure increment Δp of 200 Pa, is plotted in Fig. 23a to e. The structural response depends on t_m and on the impulse, which is defined as $I \quad \int_0^{t_l} F_{ext}(t)\,dt \quad S\int_0^{t_l} P(t)\,dt$ where t_l is the loading time, S the loading surface and $P(t)$ is the time evolution of the pressure. For $t_m \geq 0.8$ s or $I/S \geq 160 - 200$ kPa·s, the behavior of the structure is quasi static. The structural time response, which has the same shape as the imposed loading signal, is represented in Fig. 23a and b. When t_m is approximately lower than $t_{str} = 0.07$ s or

$I/S \leq 15$ kPa·s, the structural behavior develops an impulsive response (Fig. 23e and f).

Between these two areas, the structural behavior is a combination of both, leading to a dynamic response (Fig. 23c and d).

In order to compare the structural time responses to each loading signal (with different rise times) on the same graphs, the displacement time curves were adimensionalized according to time by dividing the latter by the rise time of the loading signal. Then, the area below the displacement time curve was calculated according to Eq. (12) and compared to an area of reference. The latter was obtained for a rise time t_m of 5 s corresponding to the quasi static response.

$$A^i \quad \int_0^{t_l} \frac{u^i(t)}{t_m^i}\, dt \tag{12}$$

where A^i is the area below the displacement curve and $u^i(t)$ the displacement at the top of the vertical wall, depending on time, when the structure is loaded by the i^{th} loading signal, whose rise time is t_m^i.

The result, expressed as a percentage of area difference, is plotted in Fig. 24a and b for different synthetic triangular and avalanche signals characterized by their own t_m and impulse values. The transition between the quasi static and dynamic responses was obtained for a 1% difference in area, i.e., for values of t_m around 0.7 1 s and impulses around 190 200 kPa·s.

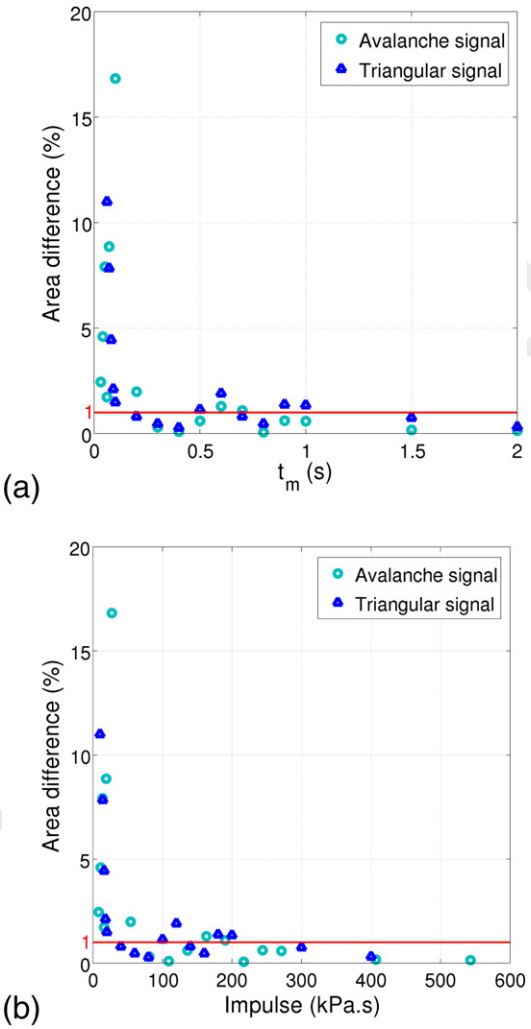

Fig. 24. Area difference of displacement-time curves according to (a) time and (b) the impulse for avalanche and triangular signals of $P_{max} = 200$ kPa.

In addition, reaction displacement curves (Fig. 25) clearly show whether or not the structural response is quasi static. In the case of a quasi static response, both curves obtained with either a pushover loading or an avalanche loading are almost the same ($t_m = 5$ s).

4.3. Pressure impulse diagram

Finally, another way to distinguish the three types of the structural response is to use pressure impulse diagrams. They describe the pressure leading to the same damage of the structure for different loading cases described by the impulse. An example of such a diagram is presented in Fig. 26a for the Taconnaz full scale wall. The corresponding damage is a 2 cm displacement at the top of the structure and the loading is the synthetic triangular signal. The three types of responses are clearly highlighted and compared to pressure impulse values of measured avalanche signals presented in Fig. 26b. Here, two events are taken into account to position them for their possibly quasi static, dynamic or impulsive influence. First, the avalanche signals observed on the Lautaret full scale avalanche test site (Thibert et al., 2013), in path no. 2 on February 9th, 2009, are reported. Rise time, maximum pressure and impulse equal 4.25 s, 162 kPa and 570 kPa·s at sensor c situated at a 1.25 meter height above ground, and 0.65 s, 194 kPa and 470 kPa·s at sensor d situated at a 1.50 meter height. Secondly, the avalanche signals measured in Vallée de la Sionne on December 4th, 2008 (Baroudi et al., 2011), are used. They were recorded at two sensors located respectively at a height of 1.5 and 2.5 m. Oppositely to the pressure signal measured at Lautaret on a 1 square meter wall set in path no. 1, these two signals were recorded by small load cells of around 100 cm^2 of surface area. In that case, rise time, maximum pressure and impulse equal 0.8 s, 264 kPa and 1176 kPa·s and 2 s, 341 kPa and 919 kPa·s, respectively.

4.4. Discussion

As shown by Paris (2010) in the field of RC structures subjected to blast loadings, three types of structural response exist: quasi static, dynamic and impulsive. For a loading signal with a maximum pressure of 200 kPa, the transition between the quasi static and the dynamic behaviors of the structure studied could be observed for an impulse around 160 200 kPa·s and the transition between dynamic and impulse behaviors for an impulse of 10 20 kPa·s. In the case of in field dense snow avalanche loadings, it seems to be necessary to know the magnitude of impulses that can be expected. For both dense snow avalanche pressure signals plotted in blue in Fig. 26b and with blue points in Fig. 26a, and also for both signals

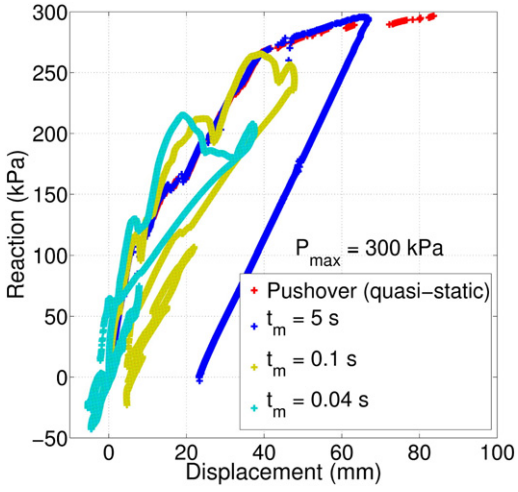

Fig. 25. Three types of structural responses to the avalanche signal with $P_{max} = 300$ kPa for several loading rates.

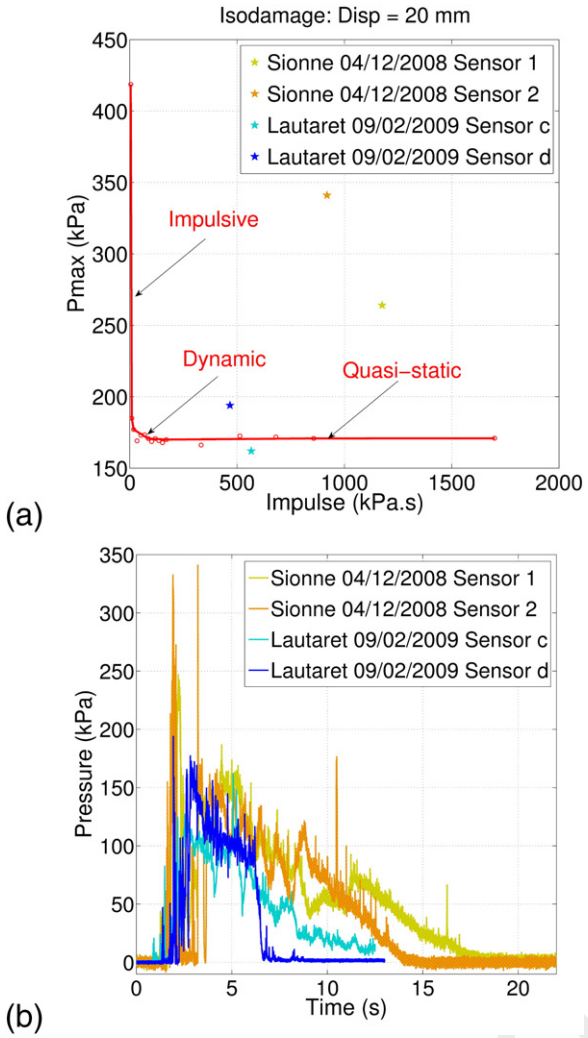

Fig. 26. (a) Pressure-impulse diagram obtained for a displacement at the top of the structure equal to 20 mm, with a synthetic triangular loading signal, compared to pressure-impulse values of actual avalanche signals and (b) pressure time plot of the avalanches used to calculate actual impulse values.

plotted in yellow, the impulses are well above 200 kPa·s, which seems to demonstrate that the response of the structure might be quasi static.

Nevertheless, in order to support this first approach, an additional study should be conducted to better account for the vertical profile of pressure which is generally observed in dense snow avalanches. This would allow deriving an impulse value which accounts for the spatial distribution of the pressure on the structure.

5. Conclusion

A 2D FE model was proposed and calibrated under quasi static conditions with experimental data to study the behavior of a protective structure subjected to a dense snow avalanche and to assess its physical vulnerability.

The FE model accounts for the same reinforcement ratio as in the experimental model and takes into account the non linear behaviors of concrete and steel. An experimental pushover test carried out on a 1/6 scale physical model allowed calibration of the model.

Four concrete constitutive laws were tested: two elasto plastic constitutive laws and two damage models. Because the loading is applied by force increments, the convergence of the algorithm is not always guaranteed. Indeed, only the Mazars damage model and the CEA model converged to the structural failure point. Moreover, while the failure mode is better described by the Mazars model, the evaluation of the ultimate pressure and displacement at failure is better represented by the CEA model.

Then, the loading signal impulse was studied to determine the contribution of the inertial effects to the structural response. The first simulations on the full scale structure subjected to avalanche loadings seem to show that the response is quasi static. An additional study examining different dense snow avalanche signals will be necessary to detail the actual impulses of such natural hazards and to confirm this preliminary conclusion. An additional improvement would also benefit from accounting for the spatial distribution of the pressure on the structure.

In the future, a reliability study of the full scale defense structure under dense avalanche loading will be conducted and more specifically the assessment of its failure probability for many maximum pressures. The CEA model will be preferred to the Mazars model, because the CPU time is lower and failure is obtained for the same experimental pressure. Fragility curves will describe the evolution of the structural failure probability according to the maximum pressure applied. This will make it possible to determine the residual risk downstream of such protective devices.

Nomenclature

α, β	Rayleigh coefficients
Δp	loading step
ϵ_{d0}	damage threshold of concrete
ϵ^c_{uc}	ultimate compressive strain of concrete
ϵ^c_{ut}	ultimate tensile strain of concrete
ϵ^s_u	ultimate strain of steel
γ_0	kinematic hardening modulus of concrete
ν^c	Poisson's ratio of concrete
ν^s	Poisson's ratio of steel
ρ^c	density of concrete
ρ^s	density of steel
a_0	nonlinear hardening modulus of concrete
A_c	material parameter of concrete describing the final assumption of the post peak stress strain curve in compression in the Mazars constitutive law
A_t	material parameter of concrete describing the final assumption of the post peak stress strain curve in tension in the Mazars constitutive law
A_{Dir}	brittleness of concrete in tension
A_{Ind}	brittleness of concrete in compression
B_c	material parameter of concrete describing the initial assumption of the post peak stress strain curve in compression in the Mazars constitutive law
B_t	material parameter of concrete describing the initial assumption of the post peak stress strain curve in tension in the Mazars constitutive law
Beta	correction factor for shear in the Mazars concrete constitutive law
Betr	reduction coefficient of shear modulus in the CEA concrete constitutive law
C	damping matrix
D	scalar damage variable of concrete
DAM1	damage in direction 1 in the CEA concrete constitutive law
E^s_h	hardening modulus of steel
E_y	Young's modulus of soil
E^c_y	Young's modulus of concrete
E^s_y	Young's modulus of steel
f^c_{cc}	biaxial compressive strength of concrete
f^c_c	compressive strength of concrete
f^c_{tr}	residual tensile strength of concrete
f^c_t	tensile strength of concrete

f_u^s	ultimate tensile strength of steel
f_y^s	yield strength of steel
Ftc	transfer factor of shear in the INSA concrete constitutive law
I_f^c	tensile brittleness index of concrete in the Mazars constitutive law
$JFIS$	cracking state indicator in the INSA concrete constitutive law
k_n	normal stiffness of joint
k_s	shear stiffness of joint
M	mass matrix
P_{max}	maximum pressure reached during loading
t_l	loading time
t_m	rise time needed to reach the maximum pressure during loading
t_{str}	characteristic time of the structural response
u	displacement of the structure

Acknowledgments

The authors are grateful to the MOPERA project funded by the French National Research Agency (ANR 09 RISK 007 01) (www.avalanches.fr/mopera projet/) for supporting this work. They thank also P. Gauer and both anonymous referees for their constructive comments that helped to improve the paper.

References

Adélaïde, L., Richard, B., Ragueneau, F., Cremona, C., 2012. A simplified numerical approach of global behaviour of RC beams degraded by corrosion. Eur. J. Environ. Civ. Eng. 16, 414–439.

Ancey, C., 1996. Guide neige et avalanches: connaissances, pratiques, sécurité. Edisud.

Baroudi, D., Thibert, E., 2009. An instrumented structure to measure avalanche impact pressure: error analysis from Monte Carlo simulations. Cold Reg. Sci. Technol. 59, 242–250.

Baroudi, D., Sovilla, B., Thibert, E., 2011. Effects of flow regime and sensor geometry on snow avalanche impact-pressure measurements. J. Glaciol. 57, 277–288.

Bazant, Z.P., Oh, B.H., 1983. Crack band theory for fracture of concrete. Mater. Struct. 93 (16), 155–177.

Berthet-Rambaud, P., 2004. Structures rigides soumises aux avalanches et chutes de blocs: modélisation du comportement mécanique et caractérisation de l'interaction "phénomène-ouvrage". Ph.D. thesis. Université Grenoble 1 — Joseph Fourier.

Berthet-Rambaud, P., Limam, A., Roenelle, P., Rapin, F., Tacnet, J.M., 2007. Avalanche action on rigid structures: back-analysis of Taconnaz deflective wall's collapse in February 1999. Cold Reg. Sci. Technol. 47, 16–31.

Berthet-Rambaud, P., Limam, A., Baroudi, D., Thibert, E., Taillandier, J.M., 2008. Characterization of avalanche loading on impacted structures: a new approach based on inverse analysis. J. Glaciol. 54, 324–332.

Bertrand, D., Naaim, M., Brun, M., 2010. Physical vulnerability of reinforced concrete buildings impacted by snow avalanches. Nat. Hazards Earth Syst. Sci. 10, 1531–1545.

Bonnevie, C., Berthet-Rambaud, P., Nicot, F., 2003. Evaluation de la vulnérabilité associée aux bâtiments en maçonnerie soumis à l'action d'une avalanche. Rev. Fr. Génie Civ. 7, 1349–1378.

Brun, M., 2002. Contribution à l'étude des effets endommageants des séismes proches et lointains sur des voiles en béton armé: Approche simplifiée couplant la dégradation des caractéristiques dynamiques avec un indicateur de dommage. Ph.D. thesis. Institut National des Sciences Appliquées, Lyon.

Brun, M., Reynouard, J.M., Jezequel, L., 2003. A simple shear wall model taking into account stiffness degradation. Eng. Struct. 25, 1–9.

Bui, T., Limam, A., Bertrand, D., Ferrier, E., 2009. Comportement des voiles en maçonnerie soumis à des chargements hors plan: Approche expérimentale et numérique par la méthode des éléments distincts. 27èmes Rencontres universitaires de l'Association Universitaire de Génie Civil, Saint-Malo.

CEN, 2005. Eurocode 2: Design of Concrete Structures — Part 1-1: General Rules and Rules for Buildings. BSI.

Daudon, D., Baroth, J., Szczurowska, P., Ying, M., Perrotin, P., 2009. Finite element models and sensibility analysis of the vulnerability of an avalanche protection gallery. International Snow Science Workshop, Davos.

Daudon, D., Baroth, J., Y., M., Perrotin, P., Mommessin, M., 2013. Sensitivity of a reinforced concrete protective gallery under a snow avalanche loading. Struct. Saf. 441, 47–56.

De Borst, R., Gutiérrez, M., 1999. A unified framework for concrete damage and fracture models including size effects. Int. J. Fract. 95, 261–277.

Favier, P., Bertrand, D., Eckert, N., Naaïm, M., 2014. A reliability assessment of physical vulnerability of reinforced concrete walls loaded by snow avalanches. Nat. Hazards Earth Syst. Sci. 14, 689–704.

Givry, M., Perfetini, P., 2006. Construire en montagne: la prise en compte du risque d'avalanche. Ministère de l'Ecologie et du Développement Durable (www.marc-givry-architecte.org).

Ile, N., Reynouard, J.M., 2000. Nonlinear analysis of reinforced concrete shear wall under earthquake loading. J. Earthq. Eng. 4, 183–213.

Ile, N., Reynouard, J.M., 2005. Behaviour of U-shaped walls subjected to uniaxial and biaxial cyclic lateral loading. J. Earthq. Eng. 9, 67–94.

La Borderie, C., 1991. Phénomènes unilatéraux dans un matériau endommageable: Modélisation et application à l'analyse des structures en béton. Ph.D. thesis. Université Paris VI, Paris, France.

Leprêtre, C., Millard, A., Combescure, A., Jamet, P., 1988. Calcul à la ruine des structures en béton armé — Mise au point d'un modèle béton en contraintes planes. Rapport DEMT 88/330. Commissariat à l'Energie Atomique, Saclay.

Mazars, J., 1986. A description of micro- and macroscale damage of concrete structures. Eng. Fract. Mech. 25, 729–737.

Merabet, O., 1990. Modélisation des structures planes en béton armé sous chargements monotone et cylique. Ph.D. thesis. Institut National des Sciences Appliquées, Lyon.

Millard, A., 1993. CASTEM 2000, Manuel d'utilisation, Rapport n° CEA-LAMBS93/007, www-cast3m.cea.fr, Saclay. Rapport CEA-LAMBS 93/007. Commissariat à l'Energie Atomique, Saclay (www.cast3m.cea.fr).

Mirza, S., MacGregor, J., 1979. Variability of mechanical properties of reinforcing bars. J. Struct. Div. 105, 921–937.

Naaïm, M., Faug, T., Naaïm, F., Eckert, N., 2010. Return period calculation and passive structure design at the Taconnaz path, France. Ann. Glaciol. 51 (54), 89–97.

Nahas, G., 1986. Calcul à la ruine des structures en béton armé. Ph.D. thesis. Université des Sciences Appliquées, Paris VI.

Paris, L., 2010. Comportement des structures soumises à une explosion. Techniques de l'ingénieur SE5064, pp. 1–26.

Pecker, A., 2010. Dynamique des structures et des ouvrages. Ecole des Ponts ParisTech.

Richard, B., 2010a. Comportement des éléments de structures en béton armé dégradés par corrosion — La problématique de l'interface acier/béton en présence de corrosion. Ph.D. thesis. Université Paris Est.

Richard, B., 2010b. Isotropic continuum damage mechanics for concrete under cyclic loading: Stiffness recovery, inelastic strains and frictional sliding. Eng. Fract. Mech. 77, 1203–1223.

Salm, B., Burkard, A., Gubler, H., 1990. Berechnung von Fliesslawinen: eine Anleitung für Praktiker mit Beispielen. Technical Report n°47. Eidgenössisches Institut für Schnee und Lawineneforschung, Davos.

Thibert, E., Baroudi, D., Limam, A., Berthet-Rambaud, P., 2008. Avalanche impact pressure on an instrumented structure. Cold Reg. Sci. Technol. 54, 206–215.

Thibert, E., Bellot, H., Ravanat, X., Ousset, F., Pulfer, G., Naaïm, M., Naaïm-Bouvet, F., Nishimura, K., Ito, Y., Baroudi, D., Prokop, A., Schön, P., Soruco, A., Vincent, C., Limam, A., Pesaresi, D., 2013. The full-scale avalanche test site, Lautaret, France. International Snow Science Workshop, Grenoble — Chamonix Mont-Blancpp. 1358–1365.